Applied Catalysis A, General 569 (2019) 141–148

Contents lists available at ScienceDirect

Applied Catalysis A, General

journal homepage: www.elsevier.com/locate/apcata

Palladium/Beta zeolite passive NOx adsorbers (PNA): Clarification of PNA chemistry and the effects of CO and zeolite crystallite size on PNA performance

Konstantin Khivantsev, Nicholas R. Jaegers, Libor Kovarik, Sebastian Prodinger, Miroslaw A. Derewinski, Yong Wang, Feng Gao, János Szanyi*

Institute for Integrated Catalysis, Pacific Northwest National Laboratory, Richland, WA, 99352, USA

ARTICLE INFO

Keywords:
Palladium
Zeolite BEA beta
Passive NOx adsorber (PNA)
Mixed carbonyl nitrosyl palladium(II) complex
High-field magic angle spinning ^{27}Al NMR

ABSTRACT

Model 0.3 wt% and 1 wt% Pd/Beta was synthesized with nano-sized Beta crystals (average size < 50 nm) and defect-free large micrometer sized crystals with similar Si/Al ratios ~13 and 15. With the aid of FTIR we reveal the formation of at least two Pd(II)–NO and one Pd(I)–NO complexes upon NO adsorption on those materials under conditions relevant to PNA. Under higher NO pressures at room temperature, we detect the formation of the first palladium(II) dinitrosyl Pd(NO)$_2$ complex, not observed previously on the solid supports or in organometallic compounds.

O_2 in dry streams promotes NO storage via additional formation of nitrosyl (NO^+) ions; it also leads to stabilization of significant amounts of N_2O_3 in BEA pores. In the presence of water, NO storage capacity is dramatically lowered. However, in the presence of CO (which is always present in exhaust gas) the performance improves. With the aid of spectroscopy and PNA measurements we show that in the presence of CO, stable mixed palladium(II) carbonyl nitrosyl complex [Pd(II)(CO)(NO)] is formed and responsible for enhanced NOx storage. This points to a general conclusion that the species responsible for NOx storage on various zeolites in the presence of water and CO, are in fact, Pd(II)(CO)(NO).

Decreasing the Pd loading to 0.3 wt% improves Pd dispersion and NO/Pd storage ratio. We also demonstrate that varying crystal sizes of BEA leads to significant changes in the NOx release temperature as well as NO/Pd ratio. Larger, defect free, more hydrophobic BEA crystals store more NOx and release it at higher temperature. Furthermore, larger, defect free and more hydrophobic BEA crystals stay significantly more active for PNA after hydrothermal aging, losing little activity compared with defective nanocrystals. High-field ^{27}Al NMR results show that larger, hydrophobic BEA crystals are more resistant to de-alumination upon hydrothermal aging (HTA), and thus are more attractive for PNA storage with Pd.

1. Introduction

Removal of toxic NO_x species from diesel engine exhaust is very important for current lean NO_x control technologies [1]. Although selective catalytic reduction (SCR) technology that relies on sacrificial urea/ammonia source is effective [2,3] at higher operating temperatures, during cold start and idle operations at temperatures below 150 °C, these materials are ineffective for the conversion of NOx to N_2 [2,3]. Lean NOx traps adsorb NOx but not continuously; furthermore, they require periodic regeneration under reducing flow [4–7]. Hence, materials to store NOx at low temperatures (< 150 °C) and release them continuously at higher temperatures (passive NOx adsorbers) when standard SCR catalysts become active, have recently been developed [8–17]. This family of materials comprises, for example, platinum dispersed on alumina and various doped/modified alumina [10,13], Pd and Pt on ceria-based materials [14]. These materials store only relatively low amounts of NOx and are somewhat susceptible, to different extent, to sulfur poisoning. Jonson Matthey, first, and then others reported Pd/zeolite formulations [11–19] on SSZ-13, BEA and ZSM-5 zeolites, with considerable NOx storage at 100 °C and NO_x release above 200 °C. The chemistry of such materials was poorly understood until recently we provided the first comprehensive molecular level insight study that identified various storage avenues for NOx on Pd/SSZ-13 model materials [19]. We showed that NO adsorption leads to the

* Corresponding author.
E-mail address: janos.szanyi@pnnl.gov (J. Szanyi).

https://doi.org/10.1016/j.apcata.2018.10.021
Received 31 August 2018; Received in revised form 17 October 2018; Accepted 20 October 2018
Available online 25 October 2018
0926-860X/

formation of Pd(II)–NO and Pd(I)–NO complexes, the latter formed by Pd(II) reduction by NO. In the presence of oxygen, Pd(I/II)–NO complexes and nitrosyl ions in ion-exchange positions of the zeolite were responsible for observed PNA promotion. When water is present in the exhaust stream, there is no agglomeration of ionic Pd but water blocks NOx adsorption sites on Pd and zeolite. We also pointed out that in the presence of CO the performance of Pd/SSZ-13 is significantly improved due to selective formation of a mixed carbonyl/nitrosyl palladium complex, Pd(II)(NO)(CO).

Pd/Beta represents another potential PNA material, with BEA showing higher resistance to structural degradation upon hydrothermal aging (HTA) at 750 °C in 10% H_2O vapor than FAU or MFI zeolite topologies (although it is fair to say that its stability is lower than SSZ-13). In recent studies [15–17] it was stated that storage of NOx under realistic conditions is due to the formation of Pd(II)–NO species and CO aids in this process by reducing Pd. Herein, we used careful FTIR measurements of NO and (NO + CO) as well as performance testing to confirm the positive effect of CO on NOx storage. Our results revealed that the formation of Pd(II)(NO)(CO) complexes and not the reduction of Pd ions in H-BEA, as previously stated, is responsible for the performance enhancement. The N–O frequencies that were previously assigned to the formation of reduced Pd–NO species are re-assigned to Pd (II)(NO)(CO) in BEA. Increasing the Pd loading in nanoBEA from 0.3 to 1 wt% decreases NO/Pd ratio due to better Pd dispersion at lower metal loadings.

Lastly, we show that NOx adsorption/release is influenced by the crystal size of the zeolite on 1 wt% Pd/BEA materials. Both the NOx release temperature and the hydrothermal stability varied with the crystallite size of the zeolite support, as evidenced by performance testing and high-field ^{27}Al NMR measurements.

2. Experimental methods

Nanosized (< 50 nm) NH_4-BEA crystals with Si/Al ~ 12.5–13 was supplied by Zeolyst. To transform it into H-form, it was calcined at 550 °C in air. Samples with 0.3 and 1 wt% Pd loading were prepared by pore volume impregnation with $[Pd(NH_3)_4](NO_3)_2$ (Sigma-Aldrich, 10%wt solution). More specifically, it was mixed with the minimum amount of water approximately equivalent to the total pore volume of the zeolite(~0.5 g of Pd-containing solution per gram zeolite was carefully and slowly pipeted onto zeolite while vigorously stirring to make sure all of zeolite gets homogeneously wet). The thick paste was mixed and stirred vigorously for 30 min, followed by calcination in air at 600 °C for 5 h (ramping rate 2 °C/min).

BEA with Si/Al ratio ~15 was synthesized in the presence of fluoride anions according to a procedure developed by Camblor et al. [20]. The gel composition was as follows SiO_2: xAl_2O_3: (0.54 + 2x)TEAOH:(0.54 + 2x)HF:(7 + 2x)H_2O. The absence of alkali cations requires only a calcination step, decomposing the organic cation (TEA^+) to convert it into Brønsted acidic H-Form [21]. 1 wt% Pd was introduced into this zeolite via a similar method.

The *in situ* static transmission IR experiments were conducted in a home-built cell housed in the sample compartment of a Bruker Vertex 80 spectrometer, equipped with an MCT detector and operated at 4 cm^{-1} resolution. The powder sample was pressed onto a tungsten mesh which, in turn, was mounted onto a copper heating assembly attached to a ceramic feedthrough. The sample could be resistively heated, and the sample temperature was monitored by a thermocouple spot welded onto the top center of the W grid. The cold finger on the glass bulb containing CO was cooled with liquid nitrogen to eliminate any contamination originating from metal carbonyls, while NO was cleaned with multiple freeze–pump–thaw cycles. Prior to spectrum collection, a background with the activated (annealed, reduced or oxidized) sample in the IR beam was collected. Each spectrum reported is obtained by averaging 256 scans.

HAADF-STEM analysis was performed with a FEI Titan 80–300 microscope operated at 300 kV. The instrument is equipped with a CEOS GmbH double-hexapole aberration corrector for the probe-forming lens, which allows for imaging with 0.1 nm resolution in scanning transmission electron microscopy mode (STEM). The images were acquired with a high angle annular dark field (HAADF) detector with inner collection angle set to 52 mrad.

^{27}Al MAS NMR measurements were performed at room temperature on a Bruker 850 MHz NMR spectrometer, operating at a magnetic field of 19.975 T. The corresponding ^{27}Al Larmor frequency is 221.412598 MHz. All spectra were acquired at a sample spinning rate of 18.7 kHz (± 5 Hz) and externally referenced to 1.0 M aqueous Al $(NO_3)_3$ (0 ppm). The advantages of both enhanced spectral resolution and sensitivity for acquiring ^{27}Al MAS NMR at ultrahigh field (19.975 T) have been established previously.

Standard NOx adsorption tests were conducted in a plug-flow reactor system with powder samples (120 mg, 60–80 mesh) loaded in a quartz tube, using a synthetic gas mixture that contained 200 ppm of NOx or (200 ppm of NOx and 14% O_2) balanced with N_2 at a flow rate of 210 sccm (corresponding to 220,000 h^{-1}, in which we consider the density of BEA to be ~2.1 g/cc). All the gas lines were heated to over 100 °C. Concentrations of reactants and products were measured by an online MKS MultiGas 2030 FTIR gas analyzer with a gas cell maintained at 191 °C. Even though it is preferable to use a pure NO feed for the study, the actual NOx feed contained ~185 ppm of NO and ~15 ppm of NO_2, where the latter came from the NO source and background NO oxidation by the heated gas lines. Since realistic engine exhausts do contain ~5% of NO_2 in the total NOx, no effort was made to remove NO_2 from our feed. Two four-way valves were used for gas switching between the reactor and the bypass. Prior to storage testing at 100 °C, the sample was pretreated in 14% O_2 balanced in N_2 flow for 1 h at 550 °C and cooled to the target temperature in the same feed. The gas mixture was then switched from the reactor to the bypass, and 200 ppm of NOx was added to the mixture. Upon stabilization, the gas mixture was switched back from bypass to the reactor for storage testing for 10 min. The sample was then heated to 600 °C at a rate of 10 °C/min to record the desorption profiles of gases in the effluent. Anaerobic NO titration experiments were also performed. Specifically, instead of switching the premixed gas from bypass to the reactor, the oxidized sample was first exposed to a flow of N_2 at a given temperature for 25 min before introducing NOx in the absence of O_2.

3. Results and discussion

3.1. NO_x storage performance of 0.3 wt% Pd/BEA in the presence of NO, NO + O_2: correlations from FTIR

Fig. 1 shows NOx trapping followed by temperature-programmed desorption (TPD) of NO_x for the 0.3 wt% Pd on H-BEA-13 zeolite with Si/Al = 12.5. We started our investigation with a 0.3 wt% Pd loaded H-BEA sample due to the fact that decreasing the loading normally decreases heterogeneity in supported catalysts. During the first 10 min of data recording, the NO_x/N_2 feed ran through the bypass line while the pre-oxidized sample (held at 100 °C) was purged with dry N_2. At t = 10 min, the feed was switched to the reactor and kept flowing through the material bed for rest of data recording. At t = 20 min, the sample temperature was started to be ramped up to 550 °C at a linear rate of 10 °C/min to desorb the trapped NO_x. The measurement was stopped shortly above 550 °C. Since the NOx inlet concentration was ~200 ppm, in the 10–20 min time-on-stream interval, the negative peaks below 200 ppm represented NO_x storage capacity, and beyond 20 min, the positive peaks above 200 ppm corresponded to NO_x released. It is evident that 0.3 wt% Pd/BEA is able to store NOx. The NO_x release is evident with a maximum amount of NO_x desorbed around 160–170 °C (~15 ppm above the NO_x baseline level). Then it levels off and a relatively broad NO_x desorption peak spanning 180–300 °C can be observed. The estimated NO/Pd ratio is ~0.4. Since only isolated Pd

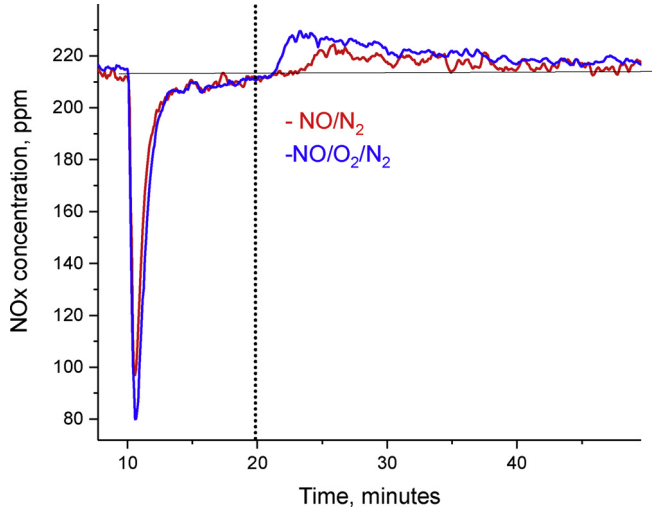

Fig. 1. NOx adsorption at 100 °C for 10 min followed with TPD (10 °C/min up to 500 °C). The feed gas mixture contains ~200 ppm of NOx (195 ppm of NO and 5 ppm of NO_2) balanced with N_2 at a flow rate of 210 sccm with or without 14% O_2. Note that during the first 10 min of data recording, the feed gas runs through a bypass line.

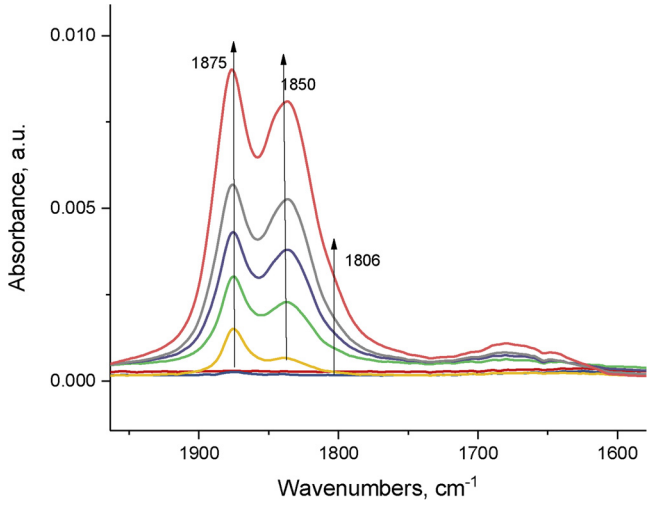

Fig. 2. FTIR of sequential NO adsorption (total aliquote 1 Torr) on pre-oxidized 0.3 wt% Pd/BEA.

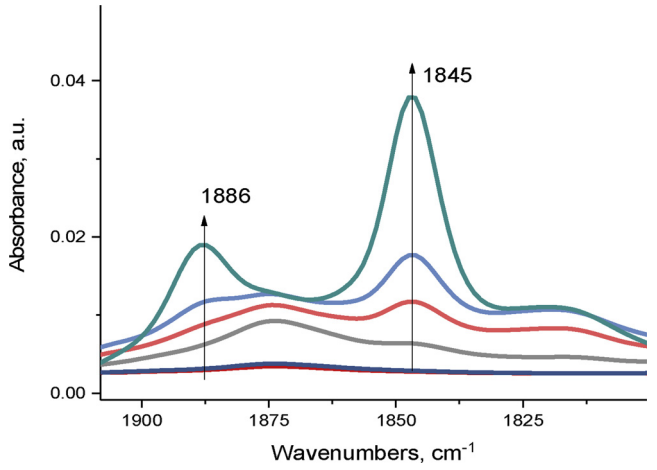

Fig. 3. FTIR of sequential NO adsorption (total aliquote ~5 Torr) on 0.3 wt% Pd/BEA pellets.

ions are active for PNA [35], this may mean two things: only ~40% of Pd is dispersed ionically in this sample, or the species involved in PNA storage are not entirely thermally stable at 100 °C, and the real dispersion of Pd is higher than 40% but the lower thermal stability of species involved in the PNA storage prevents higher NO/Pd ratio.

NO_x trapping followed by temperature-programmed desorption (TPD) for 0.3 wt% Pd on H-BEA zeolite with Si/Al = 12.5 in the presence of 14% O_2 in the gas stream (in the absence of water) is also shown in Fig. 1. The presence of oxygen clearly leads to the promotion of NO uptake by Pd/BEA: NO/Pd ratio increases to ~0.5. NO release in this case starts above 130 °C, with the release temperature extended across 130–300 °C. No significant changed are observed in the higher temperature range (> 300 °C). In case of Pd/SSZ-13, we have shown that the O_2 promotes the formation of nitrosonium NO^+ cations in ion-exchange positions of zeolite that have notable thermal stability and release NO > 150 °C [19]. It is possible that the similar phenomenon takes place here. However, NO^+ stability in this case should be lower than in the case of small-pore SSZ-13 with smaller cages and more stable NO^+ species, as we demonstrate further (Fig. 6).

In order to understand the observed changes, we turned to FTIR as it is the most sensitive technique that can provide complete speciation of M-NO species. The infra-red signature of chemisorbed NO, due to its high molar absorption coefficient [22–24], is a commonly used probe to assess the state and distribution of metal and other species present in transition metal complexes/structures dispersed on inorganic oxides. NO adsorption (1 Torr) on Pd/BEA at room temperature leads to the formation of three main absorption features corresponding to N–O stretching vibrations: 1875, 1850 and a smaller feature at 1806 cm^{-1}. In comparison with Pd/SSZ-13 where only two main features can be seen, it is obvious that the presence of a larger number of crystallographically distinct T-sites in H-BEA (as opposed to SSZ-13 which has only 1 or 2 distinguishable T-sites) leads to a more diverse speciation of these Pd mono-nitrosyls Pd(I/II)-NO (Fig. 2). We will discuss the assignment of each nitrosyl band in the following chapter.

At a higher partial pressures of NO (> 2 Torr), the doublet feature starts to grow, with bands growing in concert at 1886 and 1845 cm^{-1} (Fig. 3). Since both bands grow simultaneously and the typical asymmetric N–O stretch is higher in intensity than the symmetric one, we can assign this complex to $Pd(II)(NO)_2$ palladium dinitrosyl species [25,26]. We performed similar experiments on two different Pd/BEA pellets to confirm that the feature ~1800 cm^{-1} is not associated with $Pd(II)(NO)_2$.

Note, that this is the first Pd complex (supported or unsupported) with two nitrosyl ligands on Pd ion experimentally observed (either in organometallic compounds or on surfaces). The only other example available in the literature includes neutral palladium atoms in a solid argon matrix with two NO ligands observed at cryogenic temperatures [27]. This species could potentially contribute to PNA. However, it is immediately decomposed under vacuum and at elevated temperatures, underlining its relatively low stability. It is only stable under sufficiently high partial pressure of NO (> 1000 ppm). Therefore, $Pd(II)(NO)_2$ does not significantly contribute to PNA capacity due to its low thermal stability (PNA studies are performed at 100 °C). It is important to note that for Pd/SSZ-13 applying vacuum does not significantly affect Pd(I/II) mononitrosyl bands [19]; however, for Pd/BEA Pd–NO bands visibly decrease under similar conditions. This indicates lower stability of Pd mononitrosyls in BEA relative to SSZ-13 (Fig. 4).

Upon oxygen admission with NO (Fig. 5) the NO^+ band at 2138 cm^{-1} grows profoundly due to the following reactions [19,22,35]: N_2O_3 + 2 H-OZ → 2 NO^+ − $^-$OZ + H_2O, and Pd(II) + NO → Pd(I) + NO^+.

It is important to pay attention to the differences of Pd in BEA relative to SSZ-13. First of all, the nitosonium ion peak position is at 2138 cm^{-1}, which is significantly lower than 2170 cm^{-1} for nitrosonium ion in SSZ-13, and only slightly higher than that in ZSM-5 at

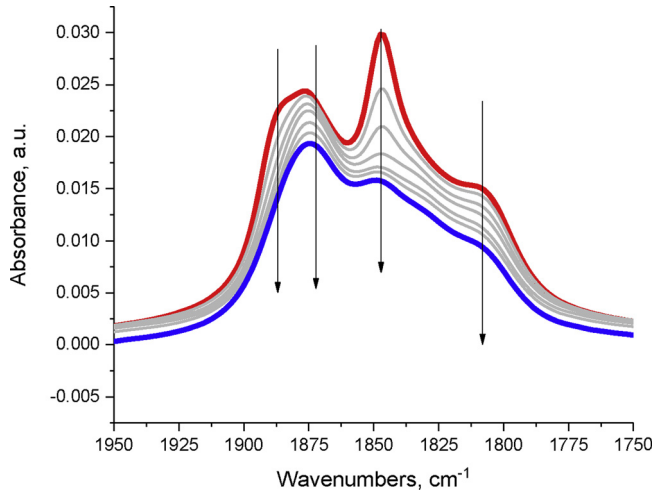

Fig. 4. FTIR of NO desorption under vacuum (up to 10^{-6} bar) from 1 Torr NO-saturated 0.3 wt% Pd/BEA.

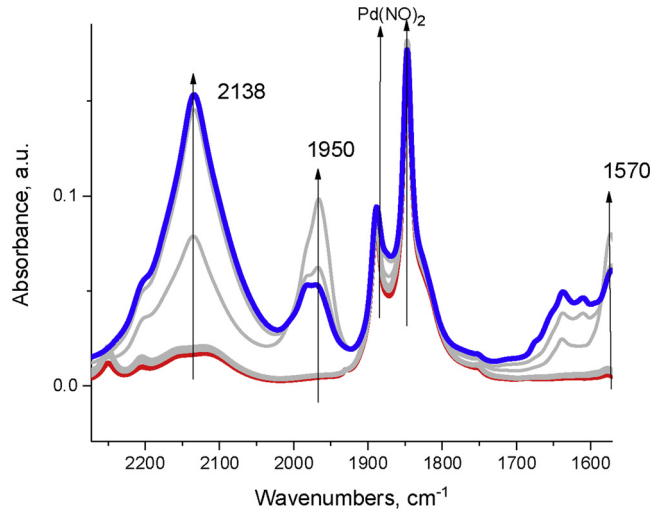

Fig. 5. FTIR of sequential (NO + O_2) adsorption on 0.3 wt% Pd/BEA.

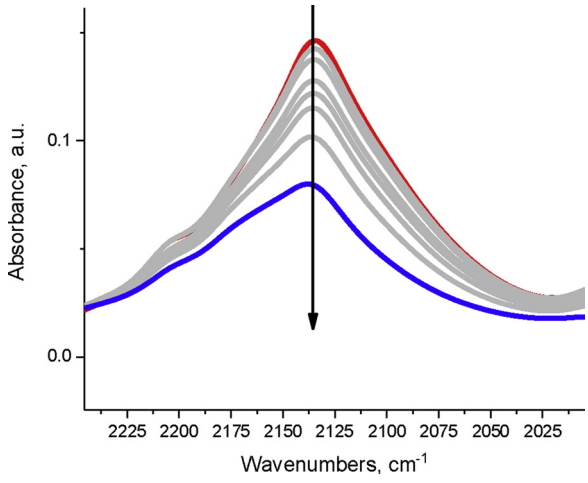

Fig. 6. FTIR of NO^+ desorption under vacuum from (NO + O_2)-saturated 0.3 wt% Pd/BEA. (Red spectrum at t = 0 and blue spectrum at t = 30 min under vacuum.) (For interpretation of the references to color in this figure legend, the reader is referred to the web version of this article).

2133 [19,22–24]. Secondly, significant amount of N_2O_3 is formed (Fig. 5, N_2O_3 bands at 1950 and 1570 cm^{-1}) whereas such species could only be transiently detected in SSZ-13 and not detected in ZSM-5. This means than BEA zeolite, unlike ZSM-5 or SSZ-13, is good at stabilizing N_2O in its micropores. Thus, our assumption of NO^+ contribution to the increased storage of NOx and its release above 130 °C is well-grounded. In this respect the system behaves similarly to Pd/SSZ-13. However, the promotion is not as significant as for SSZ-13 due to obviously lower thermal stability of NO^+ in BEA. This is evident upon evacuation of NO^+ species. Unlike NO^+ in SSZ-13, evacuation at room temperature is sufficient to decrease its population significantly, underlining its lower stability (Fig. 6).

Also, in the case of (NO + O_2), although we observe the growth of bidentate nitrate bands in the 1700 − 1600 cm^{-1} region, they do not significantly contribute to PNA as seen from PNA performance data in the presence of O_2.

3.2. NO_x storage performance of 0.3 wt% Pd/SSZ-13 in the presence of H_2O and CO and correlations from FTIR

In the presence of H_2O + O_2 and absence of CO the NO/Pd ratio drops dramatically to ~0.15, whereas it is 0.4 for just NO adsorption. Water blocks NO adsorption sites on Pd and prevents effective NOx release. In the presence of CO, peculiarly, the NO/Pd ratio increases to ~0.9 (Fig. 7).

The NOx release peak is shifted to temperatures > 190 °C. That is beneficial for PNA performance as SCR catalysts are already active at this temperature. Therefore the positive effect of CO on NOx adsorption is clearly observed. We also performed PNA with 65 ppm CO and 200 ppm CO and we observe that increasing partial pressure of CO leads to more effective PNA capacity (Fig. 8).

This is in agreement with the previous studies [15,17]. However, in those studies based on FTIR spectroscopy, it was concluded that Pd(II) gets reduced by CO and this leads to stronger NOx adsorption. Vu et al. concluded [17] that some new NO peaks formed upon adsorption of mixtures of (CO + NO + O_2) on Pd/BEA in the region ~1800 cm^{-1} belong to NO adsorbed on reduced Pd species. In that study, unfortunately, the CO region was not shown. We recently demonstrated that the sole reason why Pd/SSZ-13 is effective for PNA is due to the formation of a stable Pd(II)(CO)(NO) complex in which CO is bound linearly and datively to Pd, while NO is bound in a bent fashion forming

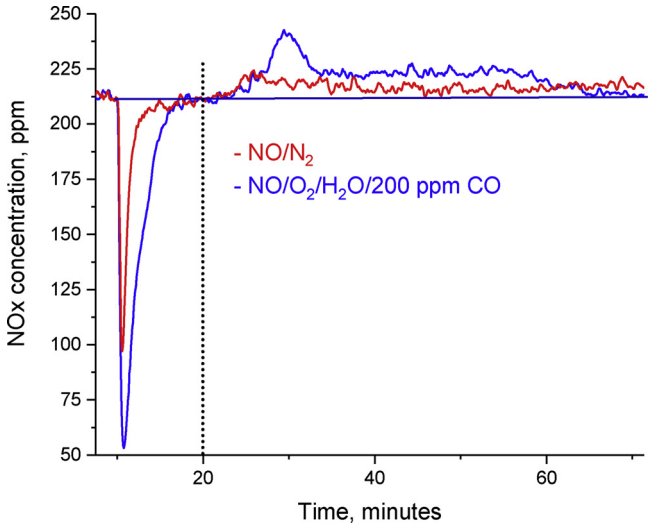

Fig. 7. NOx adsorption at 100 °C for 10 min (after 10 min bypass) followed with TPD (10 °C/min). The feed gas mixture contains ~200 ppm of NOx/N_2 or ~200 ppm NOx, 14% O_2, 3.0% H_2O with 200 ppm CO (sample mass 120 mg, total flow rate 210 sccm/min).

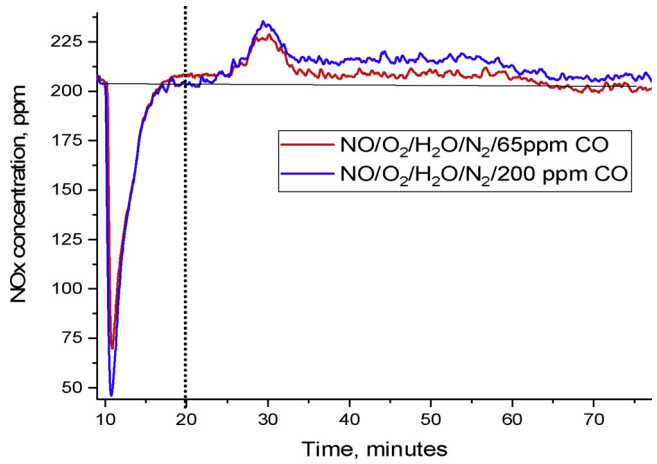

Fig. 8. NOx adsorption at 100 °C for 10 min (after 10 min bypass) followed with TPD (10 °C/min). The feed gas mixture contains ~200 ppm of NOx, 14% O_2, 3.0% H_2O with 65 or 200 ppm CO.

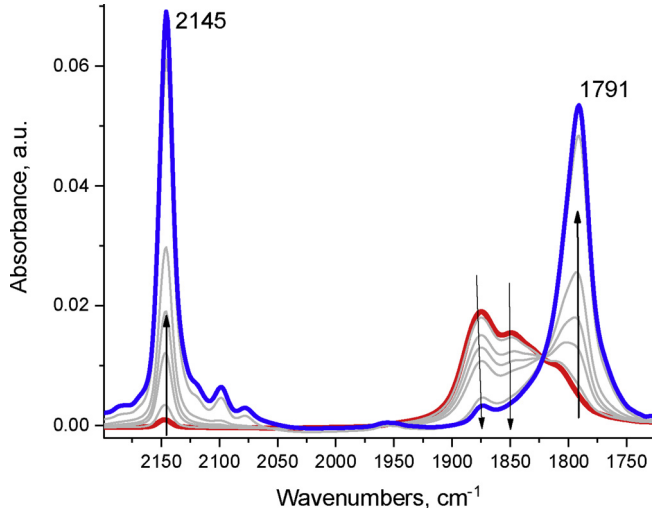

Fig. 9. FTIR of sequential CO adsorption (total aliquote ~5 Torr) on NO-saturated 0.3 wt% Pd/BEA.

a strong covalent bond with Pd [19,35]. The role of CO is basically to protect Pd from getting poisoned by water. In order to understand the observed data for Pd/BEA, we performed CO adsorption on NO-saturated Pd/BEA sample. Fig. 9 shows sequential adsorption of CO on Pd–NO palladium mononitrosyl-BEA.

The two bands that we earlier suggested were Pd(II)–NO complexes near two different crystallographically (and electronically) non-equivalent T(Al)-sites at 1875 and 1850 cm^{-1} start to go down and two relatively sharp bands start to grow with maxima at 2147 cm^{-1} and 1791 cm^{-1}. It is clear that the latter bands grow at the expense of the former two. The 2147 cm^{-1} band belongs to C–O stretch, while the 1791 cm^{-1} band lies in the typical NO stretch region. Therefore, it is logical to assume that a Pd(II)(CO)(NO) complex formed. The simultaneous decrease in the intensities of the two nitrosyl bands in order to form Pd(II)(NO)(CO) means that they could either belong to $Pd(NO)_2$ complex or they could belong to two Pd(II)–NO complexes with slightly different locations in the BEA structure. Via deduction, if they were to belong to one type $Pd(NO)_2$ then it is logical that only one type of complex grows because the bands seem relatively sharp. However, if we take a look at the magnified region of their growth, we see that both CO and NO stretches of Pd(CO)(NO) have a split nature: 2152 and 2144, as well as 1791 and 1805. This observation, in fact, directly proves that two Pd(II)–NO complexes with slightly different positions in BEA with respect to different T-sites get formed, and they get selectively transformed to two Pd(II)(CO)(NO) complexes with slightly different positions (sitting against electronically different T-sites) in BEA micropore (Fig. 10).

Upon their evacuation under high vacuum (Fig. 11), both complexes slowly lose CO and restore the original Pd(II)–NO features with the third band being at ~1805 cm^{-1}. That band does not change or interact with CO, we assign it to a stable coordinatively saturated Pd(I)–NO complex with a possibly linear $–O_{zeo}–Pd–N$ bond [19]. This once again indicates that the CO and NO bind to Pd in a different way, CO forms a dative bond and a linear Pd–C–O fragment, whereas NO, unlike usually assumed, does not bind like CO, but, instead, forms a covalent Pd–N–O fragment with a bent Pd–N–O structure [35].

This explains that what the authors have seen previously and assigned to reduction of Pd by CO [15–17] is in fact the formation of a mixed carbonyl nitrosyl Pd(II) complex. Thus we re-assess how CO promotes the NO storage: by forming a complex stable at this low temperature in which CO prevents poisoning of Pd by water. Thus, we believe the formation of a mixed carbonyl nitrosyl complex Pd(II)(NO)(CO) is a general trend for various zeolites (BEA, SSZ-13 and potentially many others) of how they are able to store NO under realistic PNA conditions where water and CO are present in the stream. NO/Pd ratio in 0.3 Pd/BEA is very high ~0.9 indicating high dispersion of Pd in this relatively low loaded sample. For just NO adsorption on 0.3 Pd/BEA the NO/Pd ratio is much lower, indicating poorer thermal stability of mononitrosyl Pd(I/II)–NO complexes compared with Pd/SSZ-13.

The next questions we sought to answer: how does the increase in Pd loading affect the NO/Pd ratio under identical conditions? In order to answer this question, we prepared 1 wt% Pd/BEA using the same IWI method starting with H-zeolite. The NO/Pd ratio in this case decreased from 0.9 to 0.6. Since NO/Pd ratio is directly proportional to the amount of atomically dispersed Pd, this indicates that in this 1 wt%

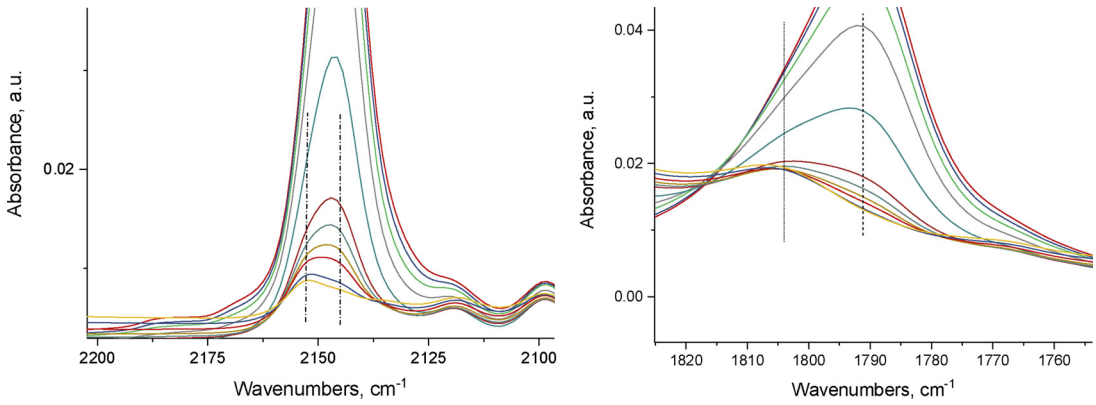

Fig. 10. FTIR of the magnified CO and NO stretching region during sequential CO adsorption (total aliquote ~5 Torr) on NO-saturated 0.3 wt% Pd/BEA.

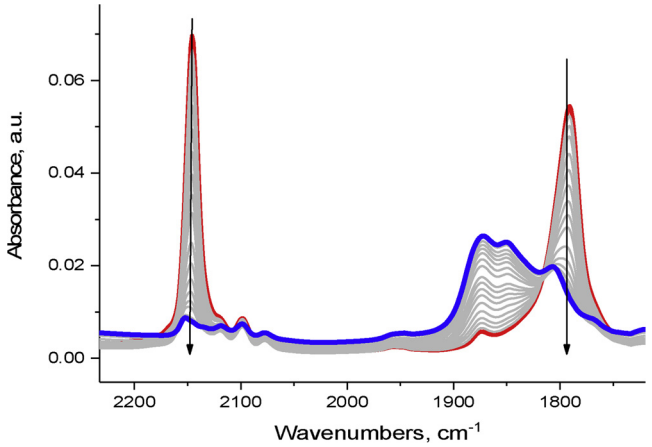

Fig. 11. FTIR of the vacuum pulled on Pd(NO)(CO) complex formed on 0.3 wt% Pd/BEA.

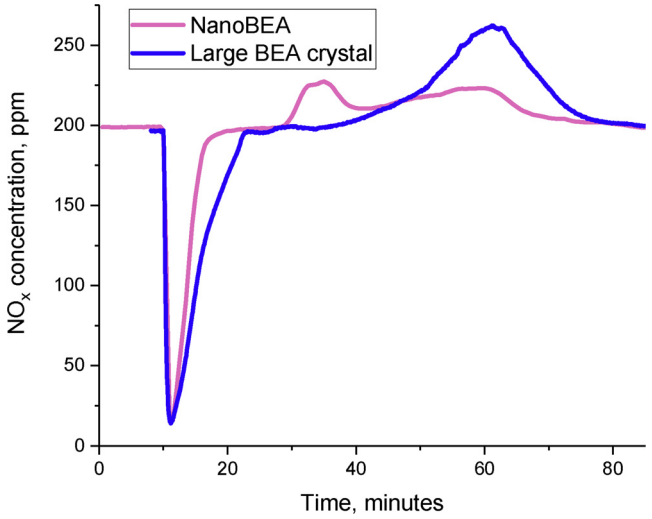

Fig. 12. NOx adsorption on 1 wt% Pd supported on nanoBEA and largeBEA at 100 °C for 10 min (after 10 min bypass) followed with TPD (10 °C/min). The feed gas mixture contains 200 ppm of NOx, 200 ppm CO, 14% O_2, 3.0% H_2O.

sample ~60% of Pd was dispersed atomically, the rest was present as PdO nanoparticles which are not active as PNA (Fig. 12). Thus, above 0.3 wt% Pd for nano-BEA support is the limit when most Pd is dispersed atomically. Above that limit the NO/Pd ratio decreases due to the inevitable agglomeration of Pd into nano PdO domains.

3.3. The effect of crystal size on PNA performance and hydrothermal stability of 1 wt% Pd/BEA

Above, we clarified the mechanism of PNA storage of Pd/BEA materials under industrially relevant PNA conditions. Zeolites are unique supports since beside their architecture the crystal size of zeolite can be tuned as well [21,28]. The effect of crystal size has not been investigated so far in regards to its effects on PNA performance. In our prior work we used commercially available BEA samples (Zeolyst) to prepare our materials: they have crystals with an average size of about 50 nm. The nanosized BEA crystals are also known to be defective. Some of us have previously devised to make large micrometer sized BEA crystals with very few defects and higher hydrophobicity utilizing hydrofluoric acid (HF) as a structure directing agent [21]. Using this route, we prepared BEA crystals with Si/Al ratio ~15 (similar to the ~13 ratio of nanosized commercially available BEA zeolites). These crystals are characterized by an average size of 8 μm (the size was

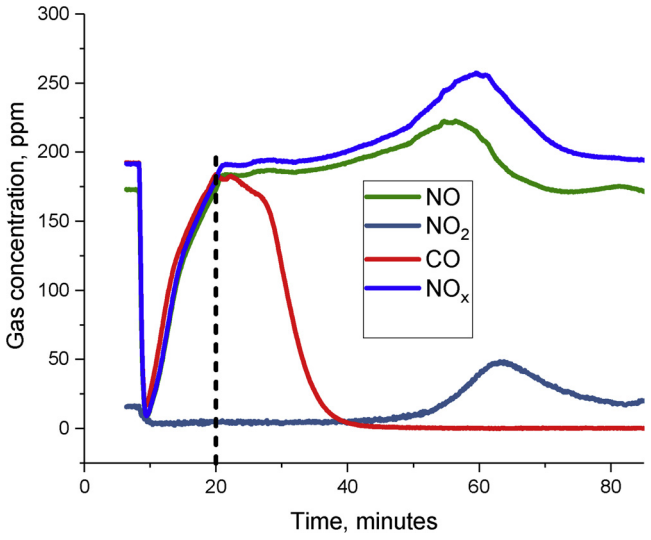

Fig. 13. Individual gas lines observed on 1 wt% Pd on largeBEA under adsorption-desorption conditions specified in Fig. 13.

previously confirmed using helium ion microscopy) and very low defect concentration and higher hydrophobicity [21].

Therefore, we chose to prepare 1 wt% Pd/BEA using exactly the same method as we used for the preparation of 1 wt% Pd/nanoBEA. The prepared material under identical PNA testing conditions showed unique features (Fig. 12).

First of all, it has higher NOx storage capacity: NO/Pd ratio increases to ~0.8. Therefore, larger and defect-free crystals are better at dispersing Pd atomically in the zeolite micropores. Second, the NO release profile at ~190 °C that is present on 1 wt% Pd/BEA is completely absent on micrometer-sized, defect free Pd/BEA. NO release starts at > 250 °C and reaches its maximum at about 450 °C. At 500 °C the maximum of NO_2 formation is observed, probably due to oxidation of NO at this temperature (Fig. 13).

Another important characteristic of PNA materials is their stability upon hydrothermal aging. We aged both 1 wt% Pd on nanoBEA and largeBEA in 10% $H_2O/O_2/N_2$ mixture for 16 h at 750 °C. After hydrothermal aging, NO/Pd ratio of Pd/nanoBEA dropped to ~0.2 (almost two times) whereas the NO/Pd ratio for Pd/largeBEA was ~0.8, close to the initial value of 0.9 (Fig. 14).

This indicates that Pd supported on larger, defect-free and more hydrophobic BEA crystals is much more resistant to hydrothermal aging than nanoBEA. Importantly, it can also be seen than in the aged sample of largeBEA a new low-temperature release peak of NOx can be seen as opposed to the fresh and very similar to the one present in defective nanoBEA crystals. See discussion regarding this vide infra.

In order to understand such changes we performed high-field magic angle spinning (MAS) ^{27}Al NMR experiments on both fresh and aged Pd/nanoBEA and largeBEA samples (Fig. 15) [29,30]. In fresh nanoBEA samples, we observe the predominant presence of various tetrahedral aluminum sites as well as some octahedral Al sites as judged by the signal around ~0 ppm. After HTA, for nanoBEA we see significant decrease in the number of T sites due to dealumination (~30–40% dealuminated) with the concomitant significant increase in penta-coordinated Al sites [29–33]. This increase in penta-coordinated Al sites coincides with the loss of PNA performance. For micrometer sized defect free, hydrophobic BEA crystals the effect of HTA is significantly less pronounced and very little aluminum is washed out of the lattice forming penta-sites, although some octahedral aluminum is obviously formed. However, the formation of this octahedrally coordinated aluminum does not lead to significant deactivation of the sample in this case as only a few penta sites can be seen.

Why does dealumination lead to decrease of PNA performance?

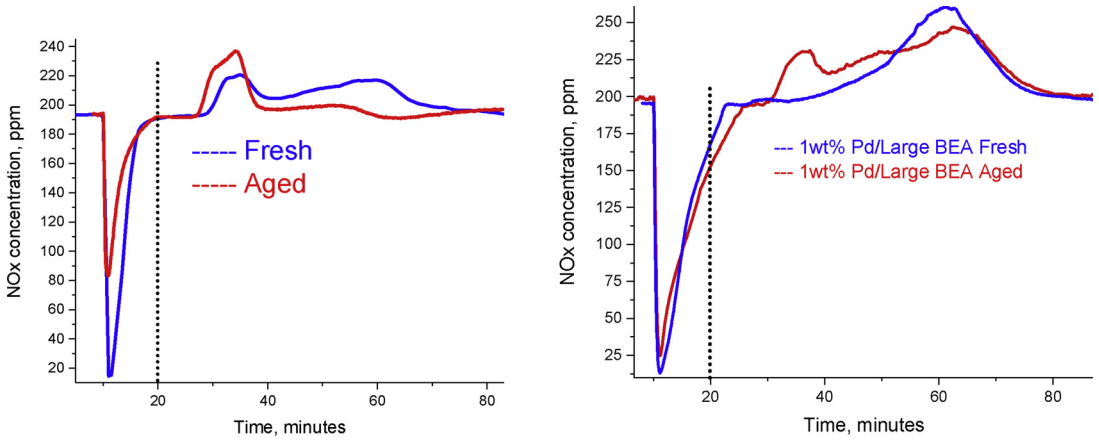

Fig. 14. Comparison of PNA performance of Fresh and Aged 1 wt% on nanoBEA and largeBEA: NOx adsorption at 100 °C for 10 min (after 10 min bypass) followed with TPD (10 °C/min). The feed gas mixture contains 200 ppm of NOx, 200 ppm CO, 14% O_2, 3.0% H_2O.

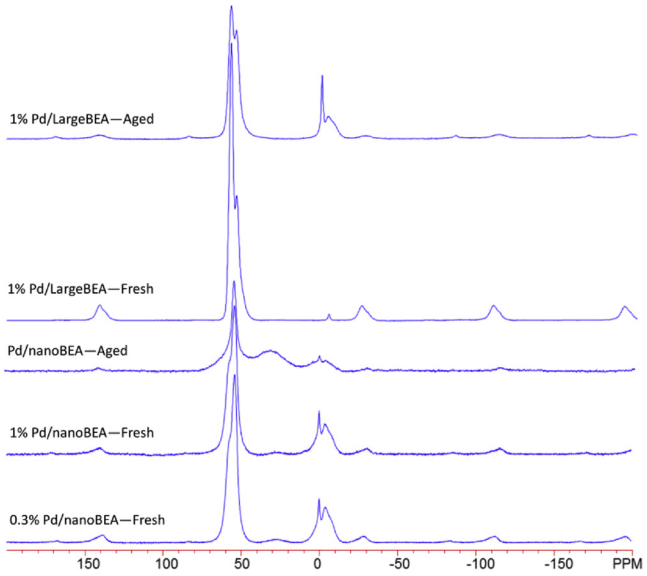

Fig. 15. High-field ^{27}Al MAS-NMR data for all prepared samples and the corresponding conditions under which MAS NMR was performed.

Let's remember that Pd sites reside near well-defined T Al sites in crystallographic positions — they hold them in atomic dispersion. As soon as those sites, associated with Pd ions, are removed from the lattice with the simultaneous formation of defect sites, Pd ions are free to move around and agglomerate into $(PdO_x)_y$ particles. Thus, we postulate that the formation of penta-Al sites during hydrothermal aging with concomitant loss of atomically dispersed Pd is the main reason for PNA deactivation on Pd/BEA. These penta-coordinated Al sites are not in the BEA zeolite framework anymore. They may be associated with inactive Pd species such as Pd ions (not in ion-exchanged positions) or PdO nanoparticles. We also observe an important feature: larger, defect-free, more hydrophobic crystals resist deactivation much better than nano-sized defective crystals, suggesting that T sites depletion takes place with ease at those defect sites. Although, largeBEA was shown to be more stable toward hot liquid water, we are not aware that it was shown to be more hydrothermally stable in prior literature, which is a notable finding. Thus, by varying crystal size we improve Pd dispersion and concomitantly NOx uptake, change the NOx release temperature and improve HTA stability of Pd/BEA PNA material. For the first time we demonstrate that varying such a simple parameter as crystal size affects Pd/zeolite PNA performance as well as hydrothermal stability and can potentially be further extended to other zeolites. The last remaining question is why does NOx release temperature split upon aging of largeBEA crystals? We note that even on Pd/nanoBEA higher temperature release feature is clearly present. The only difference between those samples is the presence of defects (microporous [34] and mesoporous) associated with octahedral Al(III) species. We speculate that some of the NOx escapes through those defective areas of the crystal whereas in the microporous sample with all NOx concentrated in the internal micropore being unable to escape through those imperfections, prevents its release at low temperature. In the aged largeBEA crystals, however, some defects appear (obviously associated with the formation of octahedral Al sites that are not associated with Pd) and low-temperature NOx release feature can now be seen.

4. Conclusions

The effect of O_2 and CO on NOx storage capacity of model Pd/BEA PNA materials was demonstrated. FTIR reveals that NO interaction with Pd/BEA yields at least two palladium(II) mononitrosyl Pd(II)–NO complexes characterized by proximity to two different T-sites as well Pd (I)–NO. At higher partial pressures of NO, the first stable palladium dinitrosyl complex $Pd(II)(NO)_2$ is formed at room temperature. This complex, however, is not expected to significantly contribute to PNA due to its lower stability compared with mononitrosyls. Addition of O_2 to NO in the absence of water vapor only marginally promotes PNA performance due to formation of nitrosonium ions NO^+ in extra-framework positions of BEA zeolite. Water addition to the lean NOx PNA stream decreases Pd/BEA PNA performance dramatically. However, CO has a strong promotional effect on PNA storage in the presence of H_2O. Previously, it has been suggested that this effect is due to CO reducing Pd ions. We show that CO promotes formation of mixed palladium carbonyl-nitrosyl complexes Pd(II)(CO)(NO) in BEA, thus improving PNA storage. This effect is the same for Pd/SSZ-13 which allows us to conclude this trend is general and Pd(II)(NO)(CO) complexes are responsible, for the most part, for PNA storage under industrially relevant conditions when CO, NO, H_2O and O_2 are present in the gas stream.

Varying crystal size of BEA significantly affects PNA performance of Pd/BEA materials: larger defect-free crystals are able to store more NOx and release it at higher temperature than defective nanoBEA. Moreover, larger (micrometer sized) defect-free and more hydrophobic BEA crystals are very resistant to hydrothermal aging. This is an important observation not only in the context of PNA applications but other potential zeolite applications such as selective catalytic reduction (SCR): although there a few examples showing that such large defect-free crystals are more tolerant to degradation in hot liquid water at temperatures not exceeding 200 °C, to the best of our knowledge, this is the

first clear example showing remarkably higher hydrothermal (aging in water vapor at 750 °C) stability of large defect-free (and more hydrophobic) zeolite crystals compared to their nanometer-sized analogues

In conclusion, we clarified the chemistry behind PNA performance of Pd/BEA materials, the effects of CO, O_2, Pd loading and crystal size on PNA performance of these materials thereby establishing clear structure-storage property relationships for the whole library of Pd/BEA materials.

Acknowledgment

We gratefully acknowledge the U.S. Department of Energy (DOE), Office of Energy Efficiency and Renewable Energy, Vehicle Technologies Program for the support of this work. Most of the research described in this paper was performed in the Environmental Molecular Sciences Laboratory (EMSL), a national scientific user facility sponsored by the DOE's Office of Biological and Environmental Research and located at the Pacific Northwest National Laboratory (PNNL). PNNL is operated for the US DOE by Battelle. S.P. and M.A.D. were supported by the Materials Synthesis and Simulation Across Scales (MS^3) Initiative conducted under the Laboratory Directed Research & Development Program at PNNL.

References

[1] M.K. Khair, W.A. Majewski, Diesel Emissions and Their Control, SAE International, Warrendale, 2006.
[2] P. Forzatti, I. Nova, E. Tronconi, Ind. Eng. Chem. Res. 49 (2010) 10386–10391.
[3] A. Beale, F. Gao, I. Lezcano-Gonzalez, C. Peden, J. Szanyi, Chem. Soc. Rev. 44 (2015) 7371–7405.
[4] W.S. Epling, L.E. Campbell, A. Yezerets, N.W. Currier, J.E. Parks, Catal. Rev. Sci. Eng. 46 (2004) 163–245.
[5] J.S. Choi, W.P. Partridge, M.J. Lance, L.R. Walker, J.A. Pihl, T.J. Toops, C.E.A. Finney, C.S. Daw, Catal. Today 151 (2010) 354–361.
[6] L. Lietti, P. Forzatti, I. Nova, E.J. Tronconi, J. Catal. 204 (2001) 175–191.
[7] D.H. Kim, K. Mudiyanselage, J. Szanyi, H. Zhu, J.H. Kwak, C.H.F. Peden, Catal. Today 184 (2012) 2–7.
[8] J.E. Melville, R.J. Brisley, O. Keane, P.R. Phillips, E.H. Mountstevens, US Patent US8105559B2, 2012.
[9] J.A. Cole, US Patent US5656244A, 1997.
[10] Y. Murata, T. Morita, K. Wada, H. Ohno, SAE Int. J. Fuels Lubr. 8 (2015) 454–459.
[11] R.R. Rajaram, H.-Y. Chen, D. Liu, US Patent US20150158019A1, 2015.
[12] H.-Y. Chen, J.E. Collier, D. Liu, L. Mantarosie, D. Duran-Martin, V. Novak, R. Rajaram, D. Thompsett, Catal. Lett. 146 (2016) 1706–1711.
[13] Y. Ji, S. Bai, M. Crocker, Appl. Catal. B Environ. 170–171 (2015) 283–292.
[14] S. Jones, Y. Ji, M. Crocker, CeO_2-M_2O_3 Passive NOx Adsorbers for Cold Start Applications, CLEERS Workshop, 2016.
[15] Y. Zheng, L. Kovarik, M.H. Engelhard, Y. Wang, Y. Wang, F. Gao, J. Szanyi, J. Phys. Chem. C 121 (2017) 15793–15803.
[16] J.R. Theis, C.K. Lambert, Catal. Today (2017), https://doi.org/10.1016/j.cattod.2017.12.014 in press.
[17] A. Vu, J. Luo, J. Li, W.S. Epling, Catal. Lett. 147 (2017) 745–750.
[18] Y. Ryou, J. Lee, H. Lee, C.H. Kim, D.H. Kim, Catal. Today (2017), https://doi.org/10.1016/j.cattod.2017.11.030 in press.
[19] K. Khivantsev, F. Gao, L. Kovarik, Y. Wang, J. Szanyi, J. Phys. Chem. C 122 (2018) 10820–10827.
[20] M.A. Camblor, A. Corma, S. Valencia, J. Mater. Chem. 8 (1998) 2137–2145.
[21] S. Prodinger, H. Shi, H. Wang, M.A. Derewinski, J.A. Lercher, Appl. Catal. B Environ. 237 (2018) 996–1002.
[22] K.I. Hadjiivanov, Catal. Rev. Sci. Eng. 42 (2000) 71–144.
[23] K. Hadjiivanov, J. Saussey, J.L. Freysz, J.C. Lavalley, Catal. Lett. 52 (1998) 103–108.
[24] J. Szanyi, M.T. Paffett, J. Catal. 164 (1996) 232–245.
[25] K. Khivantsev, A. Vityuk, H.A. Aleksandrov, G.N. Vayssilov, D. Blom, O.S. Alexeev, M.D. Amirdis, ACS Catal. 7 (2017) 5965–5982.
[26] K. Khivantsev, A. Vityuk, H.A. Aleksandrov, G.N. Vayssilov, O.S. Alexeev, M.D. Amirdis, J. Phys. Chem. C 119 (2015) 17166–17181.
[27] M.E. Alikhani, L. Krim, L. Manceron, J. Phys. Chem. A 105 (2001) 7817–7822.
[28] S. Mintova, J.P. Gilson, V. Valtchev, Nanoscale 5 (2013) 6693–6703.
[29] J.H. Kwak, J.H. Lee, S.D. Burton, A.S. Lipton, C.H.F. Peden, J. Szanyi, Angew. Chem. Int. Ed. 52 (2013) 9985–9989.
[30] L. Kovarik, N.M. Washton, R. Kukkadapu, A. Devaraj, A. Wang, Y. Wang, J. Szanyi, C.H.F. Peden, F. Gao, ACS Catal. 7 (2017) 2458–2470.
[31] F. Gao, E.D. Walter, M. Kollar, Y. Wang, J. Szanyi, C.H.F. Peden, J. Catal. 319 (2014) 1–14.
[32] N.R. Jaegers, C. Wan, M.Y. Hu, M. Vasiliu, D.A. Dixon, E. Walter, I.E. Wachs, Y. Wang, J.Z. Hu, J. Phys. Chem. C 121 (2017) 6246–6254.
[33] J.Z. Hu, X. Zhang, N.R. Jaegers, C. Wan, T.R. Graham, M. Hu, C.I. Pearce, A.R. Felmy, S.B. Clark, K.M. Rosso, J. Phys. Chem. C 121 (2017) 27555–27562.
[34] Z. Qin, K.A. Cychosz, G. Melinte, H. El Siblani, J.-P. Gilson, M. Thommes, C. Fernandez, S. Mintova, O. Ersen, V. Valtchev, J. Am. Chem. Soc. 139 (2017) 17273–17276.
[35] K. Khivantsev, N.R. Jaegers, L. Kovarik, J.C. Hanson, F.F. Tao, Y. Tang, X. Zhang, I.Z. Koleva, H.A. Aleksandrov, G.N. Vayssilov, Y. Wang, F. Gao, J. Szanyi, Angew. Chem. Int. Ed. (2018), https://doi.org/10.1002/anie.201809343.